Article

Structure

Cryo-EM structures of a bathy phytochrome histidine kinase reveal a unique light-dependent activation mechanism

Graphical abstract

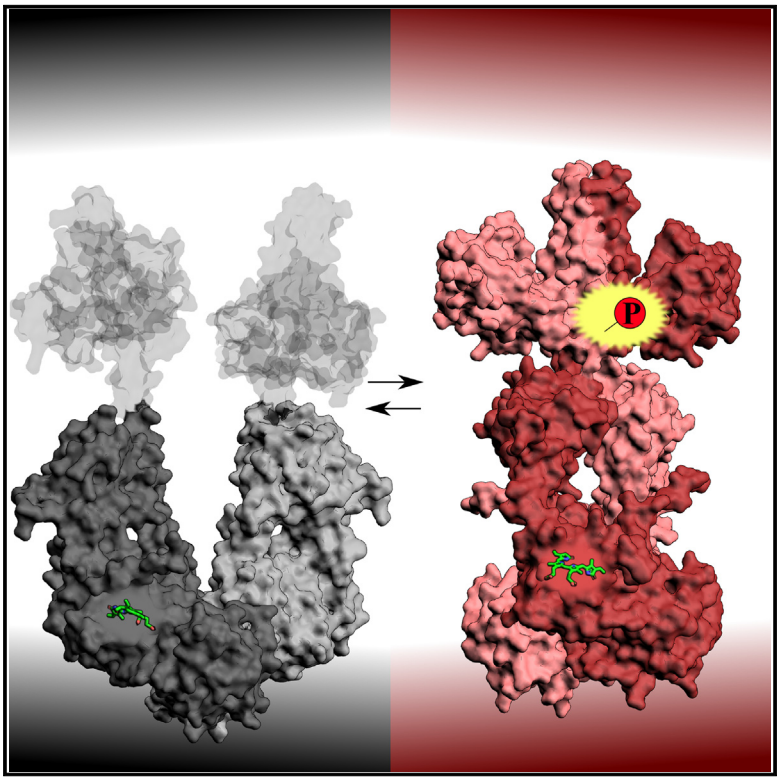

Authors

Szabolcs Bódizs, Petra Mészáros, Lukas Grunewald, Heikki Takala, Sebastian Westenhoff

Correspondence

sebastian.westenhoff@kemi.uu.se

In brief

Phytochromes are red-light photoreceptors. Bódizs et al. present the resting and activated state cryoelectron microscopy (cryo-EM) structures of a reverse-activated phytochrome consisting of a photosensory module and a histidine kinase (HK), which explain how the photosignal is transduced to the enzymatic domain and translated to a chemical signal.

Highlights

- Cryo-EM structures of a bathy bacteriophytochrome at near-atomic resolution
- Large structural changes between states lead to a strong on-off switching mechanism
- Connector region length responsible for adjusting photoresponse

Bódizs et al., 2024, Structure *32*, 1–11
November 7, 2024
https://doi.org/10.1016/j.str.2024.08.008

CellPress

Structure

CellPress
OPEN ACCESS

Article

Cryo-EM structures of a bathy phytochrome histidine kinase reveal a unique light-dependent activation mechanism

Szabolcs Bódizs,[1] Petra Mészáros,[1] Lukas Grunewald,[1] Heikki Takala,[2] and Sebastian Westenhoff[1,3,*]
[1]Department of Chemistry - BMC, Biochemistry, Uppsala University, 75123 Uppsala, Sweden
[2]Nanoscience Center, Department of Biological and Environmental Science, University of Jyväskylä, 40014 Jyväskylä, Finland
[3]Lead contact
*Correspondence: sebastian.westenhoff@kemi.uu.se
https://doi.org/10.1016/j.str.2024.08.008

SUMMARY

Phytochromes are photoreceptor proteins in plants, fungi, and bacteria. They can adopt two photochromic states with differential biochemical responses. The structural changes transducing the signal from the chromophore to the biochemical output modules are poorly understood due to challenges in capturing structures of the dynamic, full-length protein. Here, we present cryoelectron microscopy (cryo-EM) structures of the phytochrome from *Pseudomonas aeruginosa* (*Pa*BphP) in its resting (Pfr) and photoactivated (Pr) state. The kinase-active Pr state has an asymmetric, dimeric structure, whereas the kinase-inactive Pfr state opens up. This behavior is different from other known phytochromes and we explain it with the unusually short connection between the photosensory and output modules. Multiple sequence alignment of this region suggests evolutionary optimization for different modes of signal transduction in sensor proteins. The results establish a new mechanism for light-sensing by phytochrome histidine kinases and provide input for the design of optogenetic phytochrome variants.

INTRODUCTION

Life depends on light, and living organisms have evolved sophisticated systems to sense it and adjust accordingly. Phytochrome proteins enable red/far-red photoreception by converting the captured photosignal into structural changes translating to biochemical activity. In the 1950s, researchers discovered phytochromes in plants as they tried to understand how plants control periodic events, such as flowering.[1] Since then, phytochromes have been identified in many different organisms including fungi, cyanobacteria, and even non-photosynthetic bacteria.[2,3] These organisms all utilize phytochrome photosensation to control essential biological and light-dependent processes like growth, reproduction, and movement.[4]

Phytochromes function by interconverting between two distinct photochromic states: the Pr state that absorbs red light with peak absorption at 700 nm and the Pfr state that absorbs far-red light with a peak excitation at 750 nm. These two structurally different states have different signaling activities. In natural lighting, the protein exists in an equilibrium between the two states, with shifts in this equilibrium depending on the illumination conditions.[4] The structural photoconversion process between the two states and the connection of the photoequilibrium to biochemical function has raised considerable scientific interest.[5–14] Two types of phytochromes are defined based on the relative free energies of the two states: *canonical* phytochromes have a more stable Pr state, whereas *reverse-activated*, or *bathy* phytochromes have Pfr as their resting state. A deeper understanding of the photoactivation process can be applied in the design of near-infrared fluorescent markers in microscopy or optogenetic tools, where phytochrome constructs are readily used as sensory modules.[15–18]

Phytochromes have a homodimeric modular structure, typically composed of an N-terminal photosensory module and a C-terminal effector/output module (Figure 1A).[19] The photosensory module is conserved across the protein superfamily, consists of PAS (Per/Arnt/Sim), GAF (cGMP phosphodiesterase/adenylyl cyclase/FhlI), and PHY (phytochrome-specific) domains, and contains a bilin cofactor as the chromophore. A flexible loop of the PHY domain, called the PHY-tongue, undergoes considerable structural changes upon photoactivation.[5] The configuration of the output module is more variable: in many bacterial phytochromes, it features an HK (histidine kinase) unit consisting of a DHp (dimerization/histidine phosphotransfer) and a CA (catalytic ATP-binding) domain.

The first phytochrome crystal structure, comprising the PAS-GAF fragment of the *Deinococcus radiodurans* phytochrome, was obtained in 2005.[20] Subsequently, structures of the phytochrome sensory modules were acquired from Cph1 (*Syneochocystis* sp. PCC6803) and *Pa*BphP (*Pseudomonas aeruginosa*),[8,21] with structures from various other species emerging later.[5,22–29] More recently, cryoelectron microscopy (cryo-EM)

Please cite this article in press as: Bódizs et al., Cryo-EM structures of a bathy phytochrome histidine kinase reveal a unique light-dependent activation mechanism, Structure (2024), https://doi.org/10.1016/j.str.2024.08.008

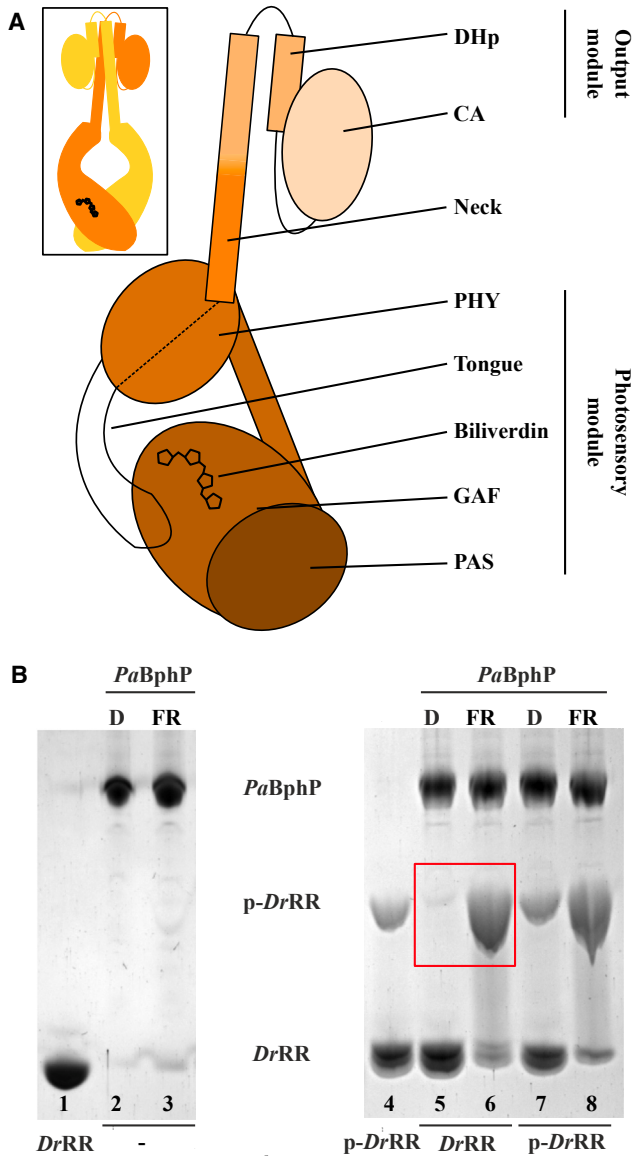

Figure 1. Schematic representation of bacterial phytochromes and the enzymatic activity of *Pa*BphP

(A) The head-to-head homodimeric configuration of the functional protein (inset), and the domain structure of a single chain. Domain abbreviations: CA, catalytic ATP-binding; DHp, dimerisation/histidine phosphotransfer; GAF, cGMP phosphodiesterase/adenylyl cyclase/Fhl1; PAS, Per/Arnt/Sim; PHY, phytochrome-specific.

(B) The enzymatic activity of *Pa*BphP, determined with Phos-tag assay, which resolves phosphorylated proteins from non-phosphorylated ones in a gel.[12] The migration of the phosphorylated response regulator from *D. radiodurans* (p-*Dr*RR) is slower than its non-phosphorylated counterpart (*Dr*RR). The samples were supplemented with identical amounts of either *Dr*RR or p-*Dr*RR, and the change in the p-*Dr*RR content speaks for net kinase (increase) or phosphatase (decrease) activity. The assay indicates that *Pa*BphP phosphorylates *Dr*RR under far-red illumination (FR) but not in the dark (D). No phosphatase activity (i.e., disappearance of p-*Dr*RR input) was detected. See Figure S2 for an extended gel.

has provided structures of plant and bacterial phytochromes with output modules.[30–33] This approach has yielded insight into the structure of phytochromes in their native full-length, dimeric forms. However, there is a scarcity of structures for bathy phytochromes and those in photoactivated states, limiting progress in understanding the photoactivation mechanism in the context of full-length phytochromes.

HK containing phytochromes are part of a two-component signaling system. Typical two-component systems consist of transmembrane sensor kinases and response regulator (RR) proteins.[34] The sensor kinases are homodimeric proteins, which detect external signals and transduce these through the membrane, thereby modulating their intracellular kinase activity.[35–38] Due to the presence of hydrophobic regions that pass the lipid bilayer, obtaining comprehensive structural information for transmembrane HKs remains challenging.[39–41] As light can pass freely through the membrane, phytochrome kinases are soluble, intracellular proteins, but have a similar structural arrangement and interdomain communication to transmembrane HKs. This makes them valuable models for investigating the signal perception and transduction mechanism in two-component systems.

An important structural element shared between transmembrane kinases and phytochrome kinases is a coiled-coil alpha helix connecting the sensor and HK modules, which we refer to as the "neck" (Figure 1A). This neck precedes the catalytic histidine of the DHp domain and plays a role in signal transduction, serving as the sole connection between the input and output modules. The neck region, defined here as spanning from the PHY domain to the catalytic histidine (H513 in *Pa*BphP), appears to be important in this signal transduction process, but its mechanism of switching between states is poorly understood.

Depending on the photochromic state, bacterial phytochromes can function as a net kinase or phosphatase. In general, phytochrome histidine kinases show kinase activity in the Pr state, whereas some phytochromes act as a phosphatase in the Pfr state.[9,11,12,42] In particular, autophosphorylation assays of the bathy phytochrome *Pa*BphP have revealed reduced kinase activity in the dark, which suggests that bathy and canonical phytochromes have a comparable activity pattern.[11,42] In cellular context the phosphate signal has to be transduced to the RR protein. *In vitro* assays targeting the phosphotransfer reaction have only been reported for some bacterial phytochromes.[12,42–45] Here, we report a characterization of this process for the bathy phytochrome *Pa*BphP.

In this study, we use single-particle cryo-EM to reveal the structure of the full-length phytochrome from *Pseudomonas aeruginosa* (*Pa*BphP) in both its Pfr and Pr state. We provide detailed structural models for the protein in both states, establishing how photoactivation works in bathy phytochromes. We identify a new mode of photo(de)activation of the output domains, and suggest that this is controlled by the constitution of the neck region. Our multiple sequence analysis on a broad range of HK-containing phytochromes highlights a potential evolutionary drive for distinct activation mechanisms.

RESULTS

PaBphP is a bathy phytochrome with kinase activity in Pr

Our ultraviolet-visible (UV-vis) spectra of *Pa*BphP confirm the bathy character of the phytochrome as it relaxes toward the Pfr state in darkness (Figure S1A).[8,46] Generally, spectra of

Please cite this article in press as: Bódizs et al., Cryo-EM structures of a bathy phytochrome histidine kinase reveal a unique light-dependent activation mechanism, Structure (2024), https://doi.org/10.1016/j.str.2024.08.008

phytochromes reflect a photo-equilibrium between the Pr and Pfr states. For canonical phytochromes, the Pfr state can never be obtained in a pure form, because the Pr state cannot be selectively photoexcited. For bathy phytochromes, dark reversion leads to accumulation of Pfr. However, even in this case, a small percentage (<10%) of the proteins is expected to remain in Pr due to thermal activation.[29,47] Nevertheless, using a bathy phytochrome provides the opportunity to obtain an almost pure Pfr state for single particle cryo-EM investigation.

To establish enzymatic activity of *Pa*BphP, we conducted a Phos-tag phosphorylation assay (Figure 1B). The assay probes if the phosphate is transduced from the phytochrome to a RR protein, which is the step that follows autophosphorylation in two-component signaling cascades. To establish this, we incubated *Pa*BphP with a phytochrome RR and ATP in the dark and under far-red (785-nm) illumination. As the cognate RR of *Pa*BphP is not known, we used the RR from *D. radiodurans* (*Dr*RR) as a substitute, which has been shown to be the phosphotransfer target of other phytochrome histidine kinases.[12] Indeed, we found out that *Pa*BphP can phosphorylate *Dr*RR in a light-controlled fashion. The phosphorylated *Dr*RR (p-*Dr*RR) fraction is enriched under far-red illumination when supplying *Dr*RR and p-*Dr*RR as a phosphorylation target (lanes 6 and 8). Moreover, the net amount of p-*Dr*RR appears unaffected by the presence of *Pa*BphP in dark (lanes 5 and 7). This indicates that *Pa*BphP acts as a net kinase and transduces the phosphate signal in Pr, but is inactive in Pfr. Compared to other bacteriophytochromes, the on/off ratio appears high.[12,48,49]

Single-particle cryo-EM structure of full-length PaBphP reveals a closed, asymmetric dimer

To link the functional changes to structure, we conducted cryo-EM on *Pa*BphP specimens prepared in the dark and under saturating far-red illumination. The illumination was supplied immediately prior to grid freezing, maximizing the concentration of Pr in these grids (Figure S1). We therefore expected that over 90% of the particles adopt Pfr in dark and Pr under far-red illumination. Single-particle cryo-EM datasets from both types were used to reconstruct near-atomic resolution structures. In the far-red illuminated (Pr) dataset, the final EM map (Figure 2A) features reliable densities across the entire length of the protein, allowing us to build an atomic model (Figure 2B). In the dark (Pfr) dataset, only the photosensory module (PAS-GAF-PHY) was resolved.

We first describe the Pr structure obtained under far-red illumination (Figure 2). In the collected dataset, 889,461 single particle images contribute to a highly homogeneous density of the photosensory module. However, there is considerable conformational heterogeneity in the output module region (Video S1), which necessitated separate local refinements of the photosensory core and output module regions (Figure S3). The local refinements were combined into a composite map (Figure 2A), which was used to reconstruct the structure (Figure 2B).

The density in the photosensory core region was reconstructed at a resolution of 3.0 Å, with densities for the chromophore and most side chains clearly visible. We find that the chromophore is in the 15Z conformation, which is expected for the Pr state (Figure 2F). The D ring is positioned near the tyrosine residues Y163 and Y190, which are in typical orientation for Pr (Figure 2D).[8,50] Moreover, D194 of the conserved PASDIP motif is within hydrogen bonding distance of R457 of the PRxSF motif, establishing contact to the PHY-tongue (Figure 2E). As expected for phytochromes in the Pr state, the tongue loop is in a β-sheet conformation (Figure 2C), with W437 making contact with the surface of the GAF domain.[5,23] The distance between D194 and G469, indicative of the length of the tongue, is 25.7 Å (Figure 2B). Interestingly, we did not find clear electron density at the position of the pyrrole water (Figure S4). The reason for this remains unclear. Even though one ordered water was visible at the acquired resolution in the electron density map (Figure S4) and the pyrrole water is typically found to have low B-factors in crystal structures, the resolution of the map is borderline with some residues showing blurred densities and no other waters in the binding pocket observed.

The density of the output module was refined separately, with an estimated resolution of ∼10 Å. The map shows clear densities for the DHp and the N box helix of the CA domain. The peptide backbone of the DHp domain can be traced through the density, allowing the determination of the degree of coiling and revealing the direction of the hairpin connecting the four helix bundle. While the CA domain has lower interpretability, the N box helix density allows the placement of a predicted structure of the domain in the envelope of the density with high confidence in the position and orientation. The full-length model of *Pa*BphP in its Pr state is shown in Figure 2B.

The structure is similar to two other structures in Pr, obtained from prototypical bacteriophytochromes.[8,50] This establishes that the Pr state of a phytochrome is similar, irrespective if the protein has Pr or Pfr as resting state. In contrast to the previous structures, we can position the DHp and CA domains with confidence. Importantly, the connecting loops between the DHp domain helices were fully resolved.[51] The loops reveal that the phosphorylation reaction will occur in between the CA domain of protomer A and catalytic histidine of protomer B (and vice versa), which is known as *trans*-autophosphorylation (Figure S5).[30,31] The orientation of the domains suggests a kinase-active state.[52]

The overall shape of the Pr dimer is asymmetric, with protomer A bent around protomer B at both dimerization interfaces (Figure 3A). While helix A (residues 118–136) of the GAF domain in protomer B assumes the orientation observed in crystal structures, the same helix in protomer A is tilted outwards at an angle of ∼13° (Figure 3B).[8] Complementing this, the neck helix of protomer A is bent significantly, resulting in the HK dimer tilting toward protomer B. Asymmetry in the dimer arrangement has been observed in plant phytochromes, but not bacterial phytochromes.[33] It may suggest a tension in the Pr state structure.

The structure of full-length PaBphP in Pfr reveals an open dimer

Now, we turn our attention to the dataset recorded in the dark. Here, two clearly distinct structures of the protein can be observed (Figure S6). A small fraction of particles (approximately 10%) show a closed conformation (marked as "closed" in Figure S6). Since the refined Pr structure overlays very well with that volume, we assign these particles to residual Pr state. The majority (90%) of the particles show a different conformation, with features expected from Pfr in the photosensory module.[8] In this state, the chromophore is in the 15E configuration

Please cite this article in press as: Bódizs et al., Cryo-EM structures of a bathy phytochrome histidine kinase reveal a unique light-dependent activation mechanism, Structure (2024), https://doi.org/10.1016/j.str.2024.08.008

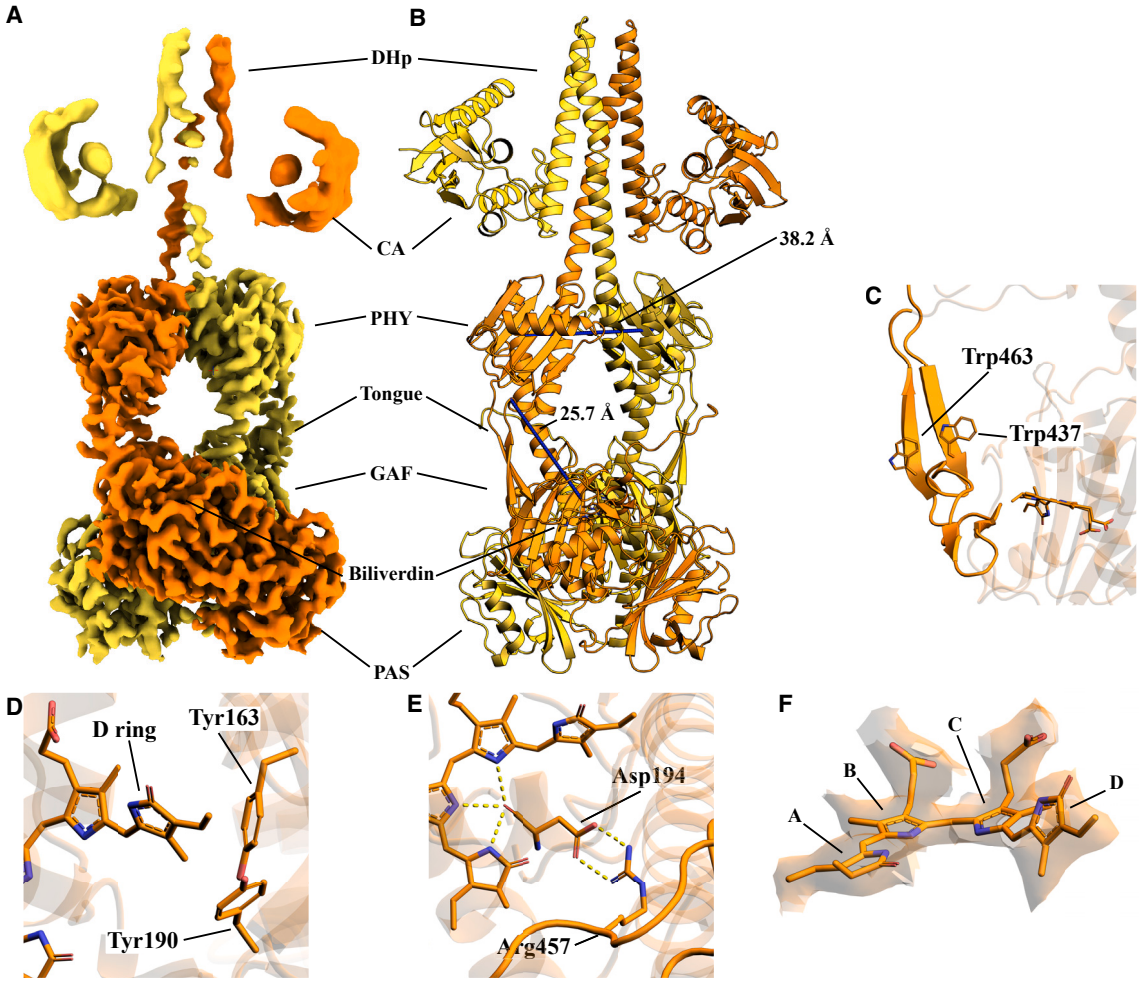

Figure 2. Structure of *Pa*BphP in its Pr state

(A) Composite EM density map (EMDB: EMD-19981) showing the full-length protein. The chains are colored differently to show coiling of the two protomers around each other.

(B) Atomic model (PDB: 9EUT) built into the density map. The PHY-tongue is extended, and the PHY domains make contact with each other.

(C) The PHY-tongue is in a β-sheet conformation, with W437 anchoring it to the GAF domain.

(D) Rotamerisation state of two tyrosine residues stabilizing the conformation of the biliverdin D ring.

(E) Polar contacts between the biliverdin, the PASDIP motif, and the PRxSF motif.

(F) The density around the biliverdin, supporting the 15Z conformation.

(Figure 4F) and the tongue loop is rearranged to an α-helical conformation (Figure 4C). In this α-helical form, W437 is positioned on the surface of the protein, and W463 takes its place in anchoring the tongue to the GAF domain.[23] The PASDIP-PRxSF connection is also rearranged compared to Pr, with D194 in contact with R453 and S459 (Figure 4E). The PHY-tongue, as measured by the D194-G469 distance (20.1 Å), is 6 Å shorter than in Pr (Figure 4B). Notably, the N-terminal strand of the loop folds into a second, shorter helix, which has not been observed in crystal structures of *Pa*BphP (Figure 5), but is present in the crystal structures of bathy phytochromes Agp2 (6G1Y) and *Rp*BphP1 (4GW9).[8,26,53]

Interestingly, the Pfr structure is open at the PHY domains, with the distance of the centroids of the PHY domains increasing by approximately 25 Å compared to Pr (Figure 4B), although the relative angle and distance of the two domains is heterogeneous (Video S2). This separation influences the entirety of the neck region: distances between residues L487 increase from 7.3 Å in Pr to 31 Å in Pfr, and the coiled-coil structure of the neck region appears disrupted. We observe a loss of signal from this region in the consensus EM density map in Pfr (Figure 4A), which we assign to the increased flexibility of the output domains in lieu of their dimer contact. Interestingly, we also find that the dimerization interface at the photosensory module changes. Helix A in protomer A assumes its relaxed orientation observed in crystal structures, rearranging the GAF dimer interface and restoring symmetry of the photosensory module (Figure 3B).[8,23] This rearrangement has not been observed in cryo-EM or crystallographic structures of bacteriophytochromes before.

The open structure is surprising in light of the two recently solved full-length structures of Pfr-state bacteriophytochromes,

Please cite this article in press as: Bódizs et al., Cryo-EM structures of a bathy phytochrome histidine kinase reveal a unique light-dependent activation mechanism, Structure (2024), https://doi.org/10.1016/j.str.2024.08.008

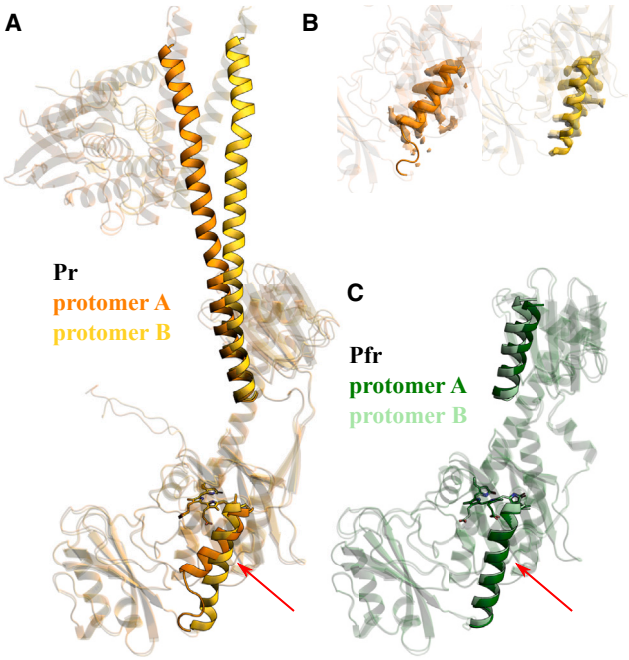

Figure 3. Symmetry in the structures of the Pr and Pfr states

The two protomers from each state were overlaid to reveal any symmetry breaking features.

(A) The Pr structure is asymmetric in the PAS/GAF region, with helix A (red arrow) and the neck of protomer A tilting toward protomer B.

(B) Density maps around helix A in protomers A/B in the Pr state support the asymmetry in the photosensory module.

(C) The Pfr structure is symmetric in the entire photosensory core module, with helix A assuming the orientation observed in crystal structures.

which showed a closed arrangement of the photosensory module dimer.[30,31] The missing densities in this dataset could in theory be explained by compositional heterogeneity. However, the reversible nature of the photocycle and the completeness of the structure in the far-red illuminated data point toward an unresolvable conformational heterogeneity instead. The presence and ratio of closed, Pr-like particles corresponds to the residual activity observed in the dark-incubated protein (Figure 1B) and the spectral features of this state (Figure S1A), further supporting the interpretation that the absence of electron density is caused by conformational heterogeneity.

The length of the neck plays a role in the structural mechanism of deactivation

Since different degrees of opening at the neck are observed for different bacteriophytochromes, we hypothesize that the constitution of the neck is responsible for the variability in this photoresponse. To investigate this, we conducted multiple sequence alignment (MSA) and analysis on the three structurally characterized and over 800 additional bacterial and fungal phytochromes that feature HK output modules. In these data we searched for patterns in the length of the neck region.

To this end, we defined a connector region that included the neck but spanned from a conserved leucine in the PHY domain (L485 in *Pa*BphP) to the catalytic histidine (H513) in the DHp (Figure 6A). The analysis reveals significant variability in this region—and hence in the neck length. The previously reported cryo-EM structures of canonical BphPs (*Dr*BphP from *D. radiodurans* and *Sa*BphP2 from *Stigmatella aurantiaca*) presented small or absent neck opening and both belong to a group with a connector length of 39 residues (Figure 6B).[30,31] In *Pa*BphP, the corresponding region is only 29 residues long, which is the shortest among all observed sequences. This group contains a number of other phytochromes from non-photosynthetic bacteria. Although the constitution of the dimer interface in the neck region will also play a role, the absence of 10 residues is a probable explanation to why *Pa*BphP opens up in Pfr while *Dr*BphP and *Sa*BphP2 do not.[30,31]

The length of the neck separates phytochromes into three clusters

We further analyzed the connector length (Figure 6) under the premise that coiled-coil linkers exhibit a full turn at a period of 7 residues, known as heptads. Given this, three separate clusters of proteins are observed, classified into separate heptad groups (l = k+n*7). Bacterial phytochromes form two clusters with l = 29(/36) residues in cluster I and l = 39(/32/46/60) residues in cluster II. The shift in connector lengths within either cluster corresponds to a full coil heptad, which likely leads to identical connections at the connecting loop of the DHp domain within a given cluster. The proteins with a connector length of l = 33 likely belong to cluster I, with an additional half heptad, or one helical turn, of the coiled-coil. An interesting cluster is observed at l = 34, which contains all analyzed fungal phytochromes and forms a separate group. *Pa*BphP, along with all known bathy bacteriophytochromes, belongs to cluster I. Overall, this analysis demonstrates an important functional role for the configuration of this connector region in terms of signaling function.

DISCUSSION

PaBphP functions as a kinase in its light-activated Pr state

Our kinase activity assay shows that *Pa*BphP is a functional HK. It was known that *Pa*BphP can autophosphorylate its catalytic H513 in Pr.[11,46] Here we establish that the protein transduces the phosphate signal in Pr to a RR protein, but that it is inactive in Pfr.[11,46] The small amount of residual enzymatic activity in dark in our assays is explained by thermal activation of the protein, which is consistent in the spectral (Figure S1A) and structural analysis (Figure S6). This residual activity is also consistent with available autophosphorylation data on bathy phytochromes. It is interesting to note that the on/off ratio is higher in *Pa*BphP compared to the prototypical phytochrome from *Agrobacterium fabrum* (Agp1), which was investigated by us using the same assay.[12] This supports the recent notion that bathy phytochromes are ideal for distinguishing between darkness and light.

The enzymatic function of *Pa*BphP is readily rationalized by our structures of the protein in Pr and Pfr. The Pr structure features a relatively stable and fully dimerized HK module, which enables the autophosphorylation reaction and phosphotransfer to the cognate RR. In Pfr, the dimer interface at the HK module is broken and this inhibits its kinase activity. This opening of the

Please cite this article in press as: Bódizs et al., Cryo-EM structures of a bathy phytochrome histidine kinase reveal a unique light-dependent activation mechanism, Structure (2024), https://doi.org/10.1016/j.str.2024.08.008

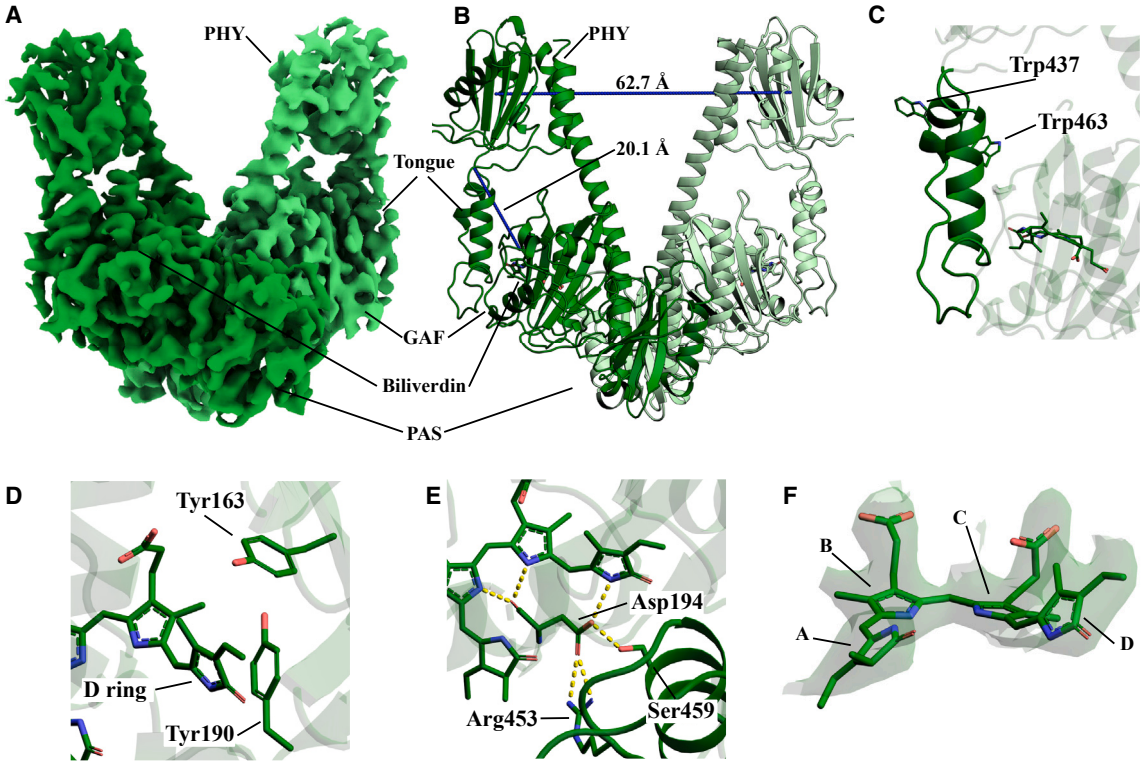

Figure 4. Structure of *Pa*BphP in its Pfr state

(A) EM density map (EMDB: EMD-19989) showing the photosensory module of the protein. The chains are colored differently to show the relative position of the two protomers. Flexibility of the DHp domain leads to complete loss of signal from the output module.

(B) Atomic model (PDB: 9EUY) built into the density map. The PHY-tongue is contracted, and the PHY domains are separated.

(C) The PHY-tongue is in an α-helical conformation, with W463 anchoring it to the GAF domain.

(D) Rotamerisation state of two tyrosine residues stabilizing the conformation of the biliverdin D ring.

(E) Polar contacts between the biliverdin, the PASDIP motif, and the PRxSF motif.

(F) The density around the biliverdin, supporting the 15E conformation.

dimer at the PHY and DHp domains readily explains the difference of biochemical function of these states.

Structure of PaBphP in its Pr state supports *trans*-autophosphorylation

Even though the HK output modules are smaller and more disordered than the photosensory modules and therefore yield consensus maps with lower resolution, the connecting loops between the DHp helices in the Pr state can be clearly traced. The positioning of the DHp four-helix bundle and the CA domain establishes *trans*-, but not *cis*-autophosphorylation of the catalytic histidine residue. The mobility of the domains (Video S1) is consistent with a recent cryo-EM structure of a transmembrane HK.[41] Likely, the mobility of the domains bears functional relevance, for example to maintain high entropy in the dimeric arrangement, to facilitate the autophosphorylation, or for the phosphate transfer reaction.

Large-scale rearrangements in the quaternary structure of PaBphP during photoactivation

The degree of structural change between Pr and Pfr states in our structures of *Pa*BphP is surprising. At the HK and PHY domains, the dimer interface breaks in Pfr, and this structural shift is supported by a rearrangement of the dimerization interface at the GAF domain. This contradicts the structural conclusions for *Pa*BphP based on modeling against time-resolved SAXS data.[54] The asymmetry in our Pr structure may indicate that the Pr state is already strained and thereby primed for opening upon photoexcitation.

The opening mechanism had been expected by extrapolation from crystal structures of bacteriophytochrome photosensory module constructs in Pr and Pfr and gel chromatography data on full-length bacteriophytochromes.[5,55] However, in subsequent SAXS and cryo-EM structures of *Dr*BphP and *Sa*BphP2, this opening was not found to occur.[5,30,31,55–57] Thus, our findings finally demonstrate a mechanism of signal transduction in a full-length phytochrome where changes close to the chromophore lead to splaying apart of the PHY and catalytic DHp domains.

The structural mechanism of (de)activation of sensor histidine kinases has been vividly debated.[35,58–61] A variety of mechanisms have been proposed, but a shortage of full-length structures has made reliable assignments difficult. Here, we find that the mechanisms can indeed be very different, even in the relatively narrow group of bacterial phytochrome kinases. Figure 7 summarizes the modes of signal transduction for the three full-length phytochromes solved by single-particle cryo-EM to

Please cite this article in press as: Bódizs et al., Cryo-EM structures of a bathy phytochrome histidine kinase reveal a unique light-dependent activation mechanism, Structure (2024), https://doi.org/10.1016/j.str.2024.08.008

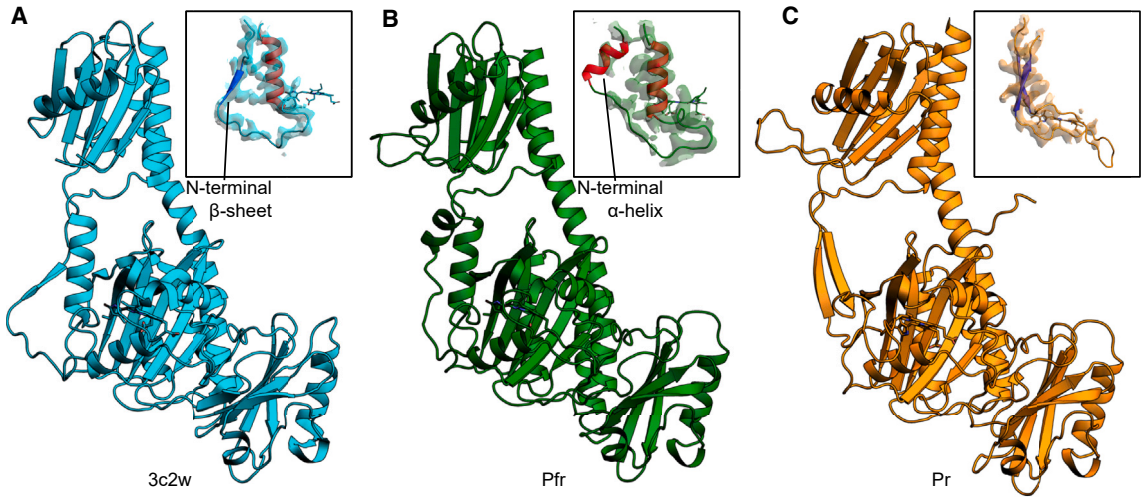

Figure 5. Comparison of the *Pa*BphP photosensory module in the crystal structure and the cryo-EM structures

(A) Crystal structure as presented by Yang et al.[8] The tongue (inset) presents a β-sheet conformation on the N-terminal strand and an α-helical conformation on the C-terminal strand, with the 2fo-fc map overlaid. This conformation is different from the one observed in the cryo-EM structure presented here, illustrating the conformational plasticity of the region.

(B) Cryo-EM structure of the protein in its Pfr state. The tongue is packed tighter, and both the N- and C-terminal strands form α-helices. Overall RMSD between the cryo-EM and crystal structures of the photosensory module is 1.08 Å.

(C) Cryo-EM structure of the protein in its Pr state. The tongue forms two antiparallel β-sheets. RMSD (excluding the output module) is 1.31 Å with the Pfr cryo-EM structure and 1.69 Å with the crystal structure.

date, which are all different. Therefore, we consider it is likely that even in the wider field of sensor histidine kinases, a variety of signal transduction mechanisms is present.[39,40,62]

Multiple sequence analysis of phytochromes reveals distinct clusters of connector regions

Our MSA analysis indicates that the variation among Pfr-state structures (Figure 7) may be caused by the differences in the neck length. Shorter necks provide less stability for the coiled-coil structure and enable complete separation of the DHp and CA domains, resulting in more reliable off-switching of the output module. It is likely that evolution has optimized the neck length to meet these requirements. In non-photoactive bacterial sensor histidine kinases, the DHp domains are connected to coiled-coil linkers, and it is reasonable to assume that a similar evolutionary optimization has taken place. Furthermore, this finding emphasizes the importance of the length and type of the connector region when designing recombinant constructs for optogenetic applications, depending on the desired outcome of photoexcitation on the output activity.

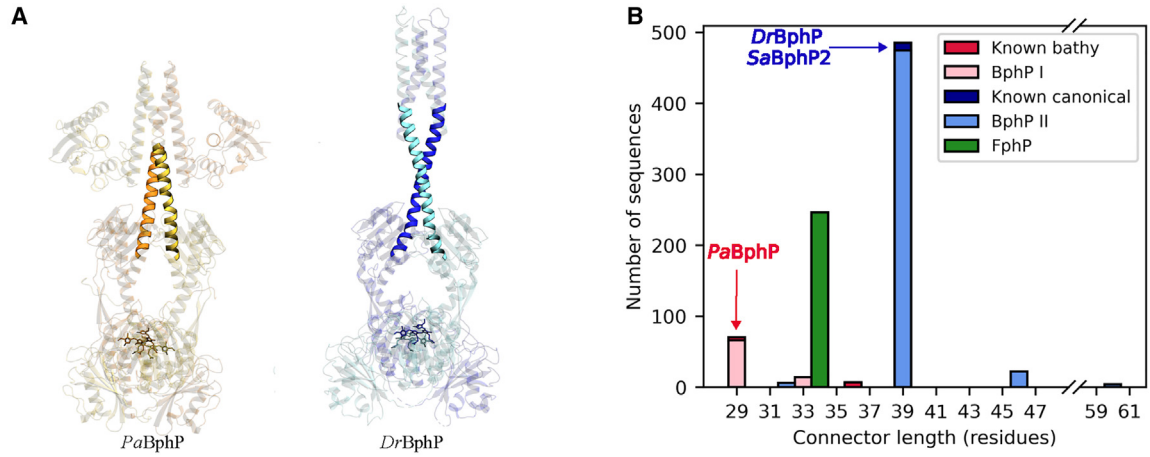

Figure 6. Distribution of the connector lengths across bacterial and fungal phytochrome HKs

(A) The structures of *Pa*BphP and *Dr*BphP with the connector regions highlighted.[30]

(B) Histogram showing the connector lengths in the analyzed sequences. Different colors represent separate clusters with connector lengths of k+n*7 residues. Proteins with known ground states are represented as darker bars, and the positions of the three bacteriophytochromes (BphP) with available full-length cryo-EM structures are indicated with arrows. Fungal phytochromes (FphP) display no variability.

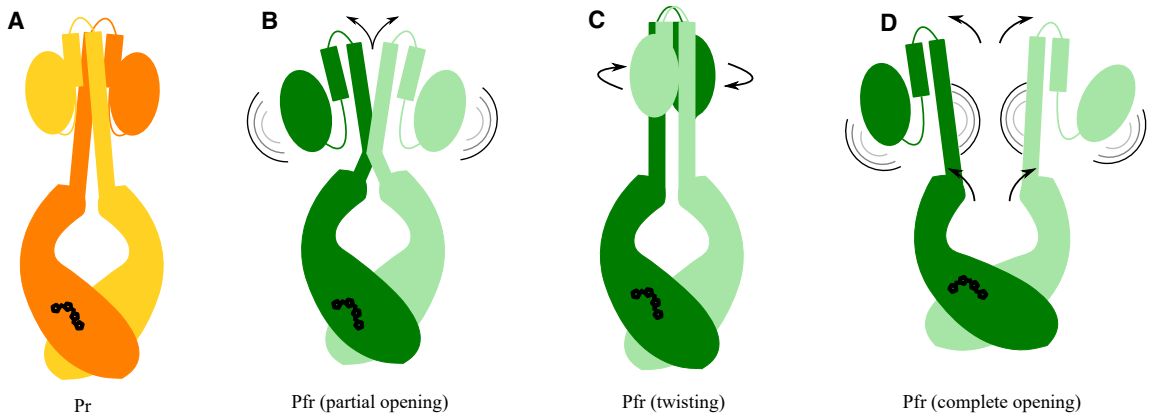

Figure 7. Proposed off-switching mechanisms for bacterial phytochromes

(A) Pr state, showing an ordered, symmetric output module.

(B) Partially opened neck, with dynamic CA domains, as seen in Pfr-state *Dr*BphP.[30]

(C) Twisted DHp domain, leading to a rearrangement of CA domain binding, as observed in Pfr-state *Sa*BphP2.[31]

(D) Open photosensory module, with highly dynamic DHp and CA domains, observed for the Pfr-state *Pa*BphP in this work.

This study presents a comprehensive structural analysis of a bathy, full-length bacteriophytochrome, elucidating the molecular basis of its light-dependent kinase activity. We have demonstrated that *Pa*BphP operates as a kinase in its Pr form, facilitated by the ordered, dimeric arrangement of the HK module, and becomes kinase-inactive upon transitioning to the Pfr state, where the sister modules separate. Our findings reveal significant large-scale structural rearrangements between these states, highlighting a novel on-off switching mechanism that is likely to have broad implications for understanding phytochrome function across bacterial species. Additionally, our sequence analysis of the neck region across a range of bacterial and fungal phytochromes suggests an evolutionary optimization of neck length for specific functional roles, offering new insights into the diversity and adaptability of phytochrome signaling mechanisms. This work integrates functional and structural examination of phytochromes and sets the stage for future explorations into the functional diversity, evolutionary history and optogenetic exploitation of this protein family.

STAR★METHODS

Detailed methods are provided in the online version of this paper and include the following:

- KEY RESOURCES TABLE
- RESOURCE AVAILABILITY
  - Lead contact
  - Materials availability
  - Data and code availability
- EXPERIMENTAL MODEL AND STUDY PARTICIPANT DETAILS
  - Source of the protein sample
  - Growth conditions for the bacterial cultures
- METHOD DETAILS
  - Protein purification
  - Spectroscopy
  - Phos-tag assay
  - Sample preparation for cryo-electron microscopy
  - Cryo-electron microscopy data collection
  - Cryo-electron microscopy data processing
  - Model building and refinement
  - Multiple sequence analysis
- QUANTIFICATION AND STATISTICAL ANALYSIS

SUPPLEMENTAL INFORMATION

Supplemental information can be found online at https://doi.org/10.1016/j.str.2024.08.008.

ACKNOWLEDGMENTS

We acknowledge the use of the Cryo-EM Uppsala facility for cryo-EM specimen preparation and screening, funded by the Department of Cell and Molecular Biology, the Disciplinary Domains of Science and Technology and of Medicine and Pharmacy at Uppsala University. We thank Daniel Larsson and Anna Sundborger-Lunna for their assistance. We thank Dr. Elina Multamäki (University of Helsinki) for her help with conducting the *Pa*BphP phosphorylation assays.

The cryo-EM data was collected at the Cryo-EM Swedish National Facility funded by the Knut and Alice Wallenberg, Family Erling Persson and Kempe Foundations, SciLifeLab, Stockholm University and Umeå University. We are grateful for the help provided by Marta Carroni, Mathieu Coincon, Julian Conrad, Dustin Morado, and Karin Walldén during data collection.

Parts of the data processing were enabled by the supercomputing resource Berzelius provided by National Supercomputer Centre at Linköping University and the Knut and Alice Wallenberg foundation.

S.W. acknowledges funding from the Swedish Research Council (grant number 2021-05101). H.T. acknowledges the Research Council of Finland (grant 330678) for funding.

AUTHOR CONTRIBUTIONS

S.W. designed the project; S.B., H.T., and S.W. planned the project and the experiments; S.B. and P.M. purified the protein; S.B. produced the grids and performed the single-particle cryo-EM data acquisition and refinement and interpreted the structures together with S.W.; H.T. performed the phosphorylation assays; L.G. performed the multiple sequence alignment; S.W. and H.T. secured funding; S.W. supervised the project; S.B., P.M., and S.W. wrote the paper with input from all authors.

DECLARATION OF INTERESTS

The authors declare no competing interests.

Received: May 13, 2024
Revised: July 5, 2024
Accepted: August 6, 2024
Published: August 30, 2024

REFERENCES

1. Butler, W.L., Norris, K.H., Siegelman, H.W., and Hendricks, S.B. (1959). Detection, assay, and preliminary purification of the pigment controlling photoresponsive development of plants. Proc. Natl. Acad. Sci. USA *45*, 1703–1708. https://doi.org/10.1073/pnas.45.12.1703.
2. Hughes, J., Lamparter, T., Mittmann, F., Hartmann, E., Gärtner, W., Wilde, A., and Börner, T. (1997). A prokaryotic phytochrome. Nature *386*, 663. https://doi.org/10.1038/386663a0.
3. Davis, S.J., Vener, A.V., and Vierstra, R.D. (1999). Bacteriophytochromes: phytochrome-like photoreceptors from nonphotosynthetic eubacteria. Science *286*, 2517–2520. https://doi.org/10.1126/science.286.5449.2517.
4. Legris, M., Ince, Y.Ç., and Fankhauser, C. (2019). Molecular mechanisms underlying phytochrome-controlled morphogenesis in plants. Nat. Commun. *10*, 5219. https://doi.org/10.1038/s41467-019-13045-0.
5. Takala, H., Björling, A., Berntsson, O., Lehtivuori, H., Niebling, S., Hoernke, M., Kosheleva, I., Henning, R., Menzel, A., Ihalainen, J.A., and Westenhoff, S. (2014). Signal amplification and transduction in phytochrome photosensors. Nature *509*, 245–248. https://doi.org/10.1038/nature13310.
6. Velazquez Escobar, F., Piwowarski, P., Salewski, J., Michael, N., Fernandez Lopez, M., Rupp, A., Qureshi, B.M., Scheerer, P., Bartl, F., Frankenberg-Dinkel, N., et al. (2015). A protonation-coupled feedback mechanism controls the signalling process in bathy phytochromes. Nat. Chem. *7*, 423–430. https://doi.org/10.1038/nchem.2225.
7. Claesson, E., Wahlgren, W.Y., Takala, H., Pandey, S., Castillon, L., Kuznetsova, V., Henry, L., Panman, M., Carrillo, M., Kübel, J., et al. (2020). The primary structural photoresponse of phytochrome proteins captured by a femtosecond X-ray laser. Elife *9*, e53514. https://doi.org/10.7554/eLife.53514.
8. Yang, X., Kuk, J., and Moffat, K. (2008). Crystal structure of Pseudomonas aeruginosa bacteriophytochrome: photoconversion and signal transduction. Proc. Natl. Acad. Sci. USA *105*, 14715–14720. https://doi.org/10.1073/pnas.0806718105.
9. Yang, X., Ren, Z., Kuk, J., and Moffat, K. (2011). Temperature-scan cryocrystallography reveals reaction intermediates in bacteriophytochrome. Nature *479*, 428–432. https://doi.org/10.1038/nature10506.
10. Ihalainen, J.A., Gustavsson, E., Schroeder, L., Donnini, S., Lehtivuori, H., Isaksson, L., Thöing, C., Modi, V., Berntsson, O., Stucki-Buchli, B., et al. (2018). Chromophore-Protein Interplay during the Phytochrome Photocycle Revealed by Step-Scan FTIR Spectroscopy. J. Am. Chem. Soc. *140*, 12396–12404. https://doi.org/10.1021/jacs.8b04659.
11. Huber, C., Strack, M., Schultheiß, I., Pielage, J., Mechler, X., Hornbogen, J., Diller, R., and Frankenberg-Dinkel, N. (2024). Darkness inhibits autokinase activity of bacterial bathy phytochromes. J. Biol. Chem. *300*, 107148. https://doi.org/10.1016/j.jbc.2024.107148.
12. Multamäki, E., Nanekar, R., Morozov, D., Lievonen, T., Golonka, D., Wahlgren, W.Y., Stucki-Buchli, B., Rossi, J., Hytönen, V.P., Westenhoff, S., et al. (2021). Comparative analysis of two paradigm bacteriophytochromes reveals opposite functionalities in two-component signaling. Nat. Commun. *12*, 4394. https://doi.org/10.1038/s41467-021-24676-7.
13. Carrillo, M., Pandey, S., Sanchez, J., Noda, M., Poudyal, I., Aldama, L., Malla, T.N., Claesson, E., Wahlgren, W.Y., Feliz, D., et al. (2021). High-resolution crystal structures of transient intermediates in the phytochrome photocycle. Structure *29*, 743–754.e4. https://doi.org/10.1016/j.str.2021.03.004.
14. Rohmer, T., Lang, C., Hughes, J., Essen, L.-O., Gärtner, W., and Matysik, J. (2008). Light-induced chromophore activity and signal transduction in phytochromes observed by 13C and 15N magic-angle spinning NMR. Proc. Natl. Acad. Sci. USA *105*, 15229–15234. https://doi.org/10.1073/pnas.0805696105.
15. Chernov, K.G., Redchuk, T.A., Omelina, E.S., and Verkhusha, V.V. (2017). Near-Infrared Fluorescent Proteins, Biosensors, and Optogenetic Tools Engineered from Phytochromes. Chem. Rev. *117*, 6423–6446. https://doi.org/10.1021/acs.chemrev.6b00700.
16. Gasser, C., Taiber, S., Yeh, C.-M., Wittig, C.H., Hegemann, P., Ryu, S., Wunder, F., and Möglich, A. (2014). Engineering of a red-light-activated human cAMP/cGMP-specific phosphodiesterase. Proc. Natl. Acad. Sci. USA *111*, 8803–8808. https://doi.org/10.1073/pnas.1321600111.
17. Tang, K., Beyer, H.M., Zurbriggen, M.D., and Gärtner, W. (2021). The Red Edge: Bilin-Binding Photoreceptors as Optogenetic Tools and Fluorescence Reporters. Chem. Rev. *121*, 14906–14956. https://doi.org/10.1021/acs.chemrev.1c00194.
18. Multamäki, E., de Fuentes, A.G., Sieryi, O., Bykov, A., Gerken, U., Ranzani, A.T., Köhler, J., Meglinski, I., Möglich, A., and Takala, H. (2022). Optogenetic Control of Bacterial Expression by Red Light. ACS Synth. Biol. *11*, 3354–3367. https://doi.org/10.1021/acssynbio.2c00259.
19. Takala, H., Edlund, P., Ihalainen, J.A., and Westenhoff, S. (2020). Tips and turns of bacteriophytochrome photoactivation. Photochem. Photobiol. Sci. *19*, 1488–1510. https://doi.org/10.1039/d0pp00117a.
20. Wagner, J.R., Brunzelle, J.S., Forest, K.T., and Vierstra, R.D. (2005). A light-sensing knot revealed by the structure of the chromophore-binding domain of phytochrome. Nature *438*, 325–331. https://doi.org/10.1038/nature04118.
21. Essen, L.-O., Mailliet, J., and Hughes, J. (2008). The structure of a complete phytochrome sensory module in the Pr ground state. Proc. Natl. Acad. Sci. USA *105*, 14709–14714. https://doi.org/10.1073/pnas.0806477105.
22. Narikawa, R., Ishizuka, T., Muraki, N., Shiba, T., Kurisu, G., and Ikeuchi, M. (2013). Structures of cyanobacteriochromes from phototaxis regulators AnPixJ and TePixJ reveal general and specific photoconversion mechanism. Proc. Natl. Acad. Sci. USA *110*, 918–923. https://doi.org/10.1073/pnas.1212098110.
23. Anders, K., Daminelli-Widany, G., Mroginski, M.A., von Stetten, D., and Essen, L.-O. (2013). Structure of the cyanobacterial phytochrome 2 photosensor implies a tryptophan switch for phytochrome signaling. J. Biol. Chem. *288*, 35714–35725. https://doi.org/10.1074/jbc.M113.510461.
24. Yang, X., Stojković, E.A., Ozarowski, W.B., Kuk, J., Davydova, E., and Moffat, K. (2015). Light Signaling Mechanism of Two Tandem Bacteriophytochromes. Structure *23*, 1179–1189. https://doi.org/10.1016/j.str.2015.04.022.
25. Nagano, S., Scheerer, P., Zubow, K., Michael, N., Inomata, K., Lamparter, T., and Krauß, N. (2016). The Crystal Structures of the N-terminal Photosensory Core Module of Agrobacterium Phytochrome Agp1 as Parallel and Anti-parallel Dimers. J. Biol. Chem. *291*, 20674–20691. https://doi.org/10.1074/jbc.M116.739136.
26. Schmidt, A., Sauthof, L., Szczepek, M., Lopez, M.F., Escobar, F.V., Qureshi, B.M., Michael, N., Buhrke, D., Stevens, T., Kwiatkowski, D., et al. (2018). Structural snapshot of a bacterial phytochrome in its functional intermediate state. Nat. Commun. *9*, 4912–4913. https://doi.org/10.1038/s41467-018-07392-7.
27. Lim, S., Yu, Q., Gottlieb, S.M., Chang, C.-W., Rockwell, N.C., Martin, S.S., Madsen, D., Lagarias, J.C., Larsen, D.S., and Ames, J.B. (2018). Correlating structural and photochemical heterogeneity in cyanobacteriochrome NpR6012g4. Proc. Natl. Acad. Sci. USA *115*, 4387–4392. https://doi.org/10.1073/pnas.1720682115.
28. Nagano, S., Guan, K., Shenkutie, S.M., Feiler, C., Weiss, M., Kraskov, A., Buhrke, D., Hildebrandt, P., and Hughes, J. (2020). Structural insights into photoactivation and signalling in plant phytochromes. Nat. Plants *6*, 581–588. https://doi.org/10.1038/s41477-020-0638-y.
29. Isaksson, L., Gustavsson, E., Persson, C., Brath, U., Vrhovac, L., Karlsson, G., Orekhov, V., and Westenhoff, S. (2021). Signaling Mechanism of Phytochromes in Solution. Structure *29*, 151–160.e3. https://doi.org/10.1016/j.str.2020.08.009.

30. Wahlgren, W.Y., Claesson, E., Tuure, I., Trillo-Muyo, S., Bódizs, S., Ihalainen, J.A., Takala, H., and Westenhoff, S. (2022). Structural mechanism of signal transduction in a phytochrome histidine kinase. Nat. Commun. *13*, 7673. https://doi.org/10.1038/s41467-022-34893-3.

31. Malla, T.N., Hernandez, C., Menendez, D., Bizhga, D., Mendez, J.H., Muniyappan, S., Schwander, P., Stojković, E.A., and Schmidt, M. (2023). Signal Transduction in an Enzymatic Photoreceptor Revealed by Cryo-Electron Microscopy. Preprint at bioRxiv. https://doi.org/10.1101/2023.11.08.566274.

32. Burgie, E.S., Li, H., Gannam, Z.T.K., McLoughlin, K.E., Vierstra, R.D., and Li, H. (2023). The structure of Arabidopsis phytochrome A reveals topological and functional diversification among the plant photoreceptor isoforms. Nat. Plants *9*, 1116–1129. https://doi.org/10.1038/s41477-023-01435-8.

33. Li, H., Burgie, E.S., Gannam, Z.T.K., Li, H., and Vierstra, R.D. (2022). Plant phytochrome B is an asymmetric dimer with unique signalling potential. Nature *604*, 127–133. https://doi.org/10.1038/s41586-022-04529-z.

34. Wolanin, P.M., Thomason, P.A., and Stock, J.B. (2002). Histidine protein kinases: key signal transducers outside the animal kingdom. Genome Biol. *3*, REVIEWS3013. https://doi.org/10.1186/gb-2002-3-10-reviews3013.

35. Bhate, M.P., Molnar, K.S., Goulian, M., and DeGrado, W.F. (2015). Signal transduction in histidine kinases: insights from new structures. Structure *23*, 981–994. https://doi.org/10.1016/j.str.2015.04.002.

36. Gushchin, I., Melnikov, I., Polovinkin, V., Ishchenko, A., Yuzhakova, A., Buslaev, P., Bourenkov, G., Grudinin, S., Round, E., Balandin, T., et al. (2017). Mechanism of transmembrane signaling by sensor histidine kinases. Science *356*, eaah6345. https://doi.org/10.1126/science.aah6345.

37. Stock, A.M., Robinson, V.L., and Goudreau, P.N. (2000). Two-Component Signal Transduction. Annu. Rev. Biochem. *69*, 183–215. https://doi.org/10.1146/annurev.biochem.69.1.183.

38. Krell, T., Lacal, J., Busch, A., Silva-Jiménez, H., Guazzaroni, M.-E., and Ramos, J.L. (2010). Bacterial Sensor Kinases: Diversity in the Recognition of Environmental Signals. Annu. Rev. Microbiol. *64*, 539–559. https://doi.org/10.1146/annurev.micro.112408.134054.

39. Mensa, B., Polizzi, N.F., Molnar, K.S., Natale, A.M., Lemmin, T., and DeGrado, W.F. (2021). Allosteric mechanism of signal transduction in the two-component system histidine kinase PhoQ. Elife *10*, e73336. https://doi.org/10.7554/eLife.73336.

40. Berntsson, O., Diensthuber, R.P., Panman, M.R., Björling, A., Gustavsson, E., Hoernke, M., Hughes, A.J., Henry, L., Niebling, S., Takala, H., et al. (2017). Sequential conformational transitions and α-helical supercoiling regulate a sensor histidine kinase. Nat. Commun. *8*, 284. https://doi.org/10.1038/s41467-017-00300-5.

41. George, N.L., and Orlando, B.J. (2023). Architecture of a complete Bce-type antimicrobial peptide resistance module. Nat. Commun. *14*, 3896. https://doi.org/10.1038/s41467-023-39678-w.

42. Mukherjee, S., Jemielita, M., Stergioula, V., Tikhonov, M., and Bassler, B.L. (2019). Photosensing and quorum sensing are integrated to control Pseudomonas aeruginosa collective behaviors. PLoS Biol. *17*, e3000579. https://doi.org/10.1371/journal.pbio.3000579.

43. Bhoo, S.-H., Davis, S.J., Walker, J., Karniol, B., and Vierstra, R.D. (2001). Bacteriophytochromes are photochromic histidine kinases using a biliverdin chromophore. Nature *414*, 776–779. https://doi.org/10.1038/414776a.

44. Karniol, B., and Vierstra, R.D. (2003). The pair of bacteriophytochromes from Agrobacterium tumefaciens are histidine kinases with opposing photobiological properties. Proc. Natl. Acad. Sci. USA *100*, 2807–2812. https://doi.org/10.1073/pnas.0437914100.

45. Baker, A.W., Satyshur, K.A., Morales, N.M., and Forest, K.T. (2016). Arm-in-Arm Response Regulator Dimers Promote Intermolecular Signal Transduction. J. Bacteriol. *198*, 1218–1229. https://doi.org/10.1128/jb.00872-15.

46. Tasler, R., Moises, T., and Frankenberg-Dinkel, N. (2005). Biochemical and spectroscopic characterization of the bacterial phytochrome of Pseudomonas aeruginosa. FEBS J. *272*, 1927–1936. https://doi.org/10.1111/j.1742-4658.2005.04623.x.

47. Lenngren, N., Edlund, P., Takala, H., Stucki-Buchli, B., Rumfeldt, J., Peshev, I., Häkkänen, H., Westenhoff, S., and Ihalainen, J.A. (2018). Coordination of the biliverdin D-ring in bacteriophytochromes. Phys. Chem. Chem. Phys. *20*, 18216–18225. https://doi.org/10.1039/c8cp01696h.

48. Lamparter, T., Michael, N., Mittmann, F., and Esteban, B. (2002). Phytochrome from Agrobacterium tumefaciens has unusual spectral properties and reveals an N-terminal chromophore attachment site. Proc. Natl. Acad. Sci. USA *99*, 11628–11633. https://doi.org/10.1073/pnas.152263999.

49. Giraud, E., Zappa, S., Vuillet, L., Adriano, J.-M., Hannibal, L., Fardoux, J., Berthomieu, C., Bouyer, P., Pignol, D., and Verméglio, A. (2005). A new type of bacteriophytochrome acts in tandem with a classical bacteriophytochrome to control the antennae synthesis in Rhodopseudomonas palustris. J. Biol. Chem. *280*, 32389–32397. https://doi.org/10.1074/jbc.M506890200.

50. Yang, X., Kuk, J., and Moffat, K. (2009). Conformational differences between the Pfr and Pr states in Pseudomonas aeruginosa bacteriophytochrome. Proc. Natl. Acad. Sci. USA *106*, 15639–15644. https://doi.org/10.1073/pnas.0902178106.

51. Ashenberg, O., Keating, A.E., and Laub, M.T. (2013). Helix Bundle Loops Determine Whether Histidine Kinases Autophosphorylate in cis or in trans. J. Mol. Biol. *425*, 1198–1209. https://doi.org/10.1016/j.jmb.2013.01.011.

52. Casino, P., Miguel-Romero, L., and Marina, A. (2014). Visualizing autophosphorylation in histidine kinases. Nat. Commun. *5*, 3258. https://doi.org/10.1038/ncomms4258.

53. Bellini, D., and Papiz, M.Z. (2012). Structure of a Bacteriophytochrome and Light-Stimulated Protomer Swapping with a Gene Repressor. Structure *20*, 1436–1446. https://doi.org/10.1016/j.str.2012.06.002.

54. Lee, S.J., Kim, T.W., Kim, J.G., Yang, C., Yun, S.R., Kim, C., Ren, Z., Kumarapperuma, I., Kuk, J., Moffat, K., et al. (2022). Light-induced protein structural dynamics in bacteriophytochrome revealed by time-resolved x-ray solution scattering. Sci. Adv. *8*, eabm6278. https://doi.org/10.1126/sciadv.abm6278.

55. Takala, H., Björling, A., Linna, M., Westenhoff, S., and Ihalainen, J.A. (2015). Light-induced Changes in the Dimerization Interface of Bacteriophytochromes. J. Biol. Chem. *290*, 16383–16392. https://doi.org/10.1074/jbc.M115.650127.

56. Burgie, E.S., Wang, T., Bussell, A.N., Walker, J.M., Li, H., and Vierstra, R.D. (2014). Crystallographic and electron microscopic analyses of a bacterial phytochrome reveal local and global rearrangements during photoconversion. J. Biol. Chem. *289*, 24573–24587. https://doi.org/10.1074/jbc.M114.571661.

57. Björling, A., Berntsson, O., Lehtivuori, H., Takala, H., Hughes, A.J., Panman, M., Hoernke, M., Niebling, S., Henry, L., Henning, R., et al. (2016). Structural photoactivation of a full-length bacterial phytochrome. Sci. Adv. *2*, e1600920. https://doi.org/10.1126/sciadv.1600920.

58. Casino, P., Rubio, V., and Marina, A. (2009). Structural insight into partner specificity and phosphoryl transfer in two-component signal transduction. Cell *139*, 325–336. https://doi.org/10.1016/j.cell.2009.08.032.

59. Diensthuber, R.P., Bommer, M., Gleichmann, T., and Möglich, A. (2013). Full-length structure of a sensor histidine kinase pinpoints coaxial coiled coils as signal transducers and modulators. Structure *21*, 1127–1136. https://doi.org/10.1016/j.str.2013.04.024.

60. Ferris, H.U., Dunin-Horkawicz, S., Hornig, N., Hulko, M., Martin, J., Schultz, J.E., Zeth, K., Lupas, A.N., and Coles, M. (2012). Mechanism of regulation of receptor histidine kinases. Structure *20*, 56–66. https://doi.org/10.1016/j.str.2011.11.014.

61. Wang, C., Sang, J., Wang, J., Su, M., Downey, J.S., Wu, Q., Wang, S., Cai, Y., Xu, X., Wu, J., et al. (2013). Mechanistic insights revealed by the crystal structure of a histidine kinase with signal transducer and sensor domains. PLoS Biol. *11*, e1001493. https://doi.org/10.1371/journal.pbio.1001493.

62. Jacob-Dubuisson, F., Mechaly, A., Betton, J.-M., and Antoine, R. (2018). Structural insights into the signalling mechanisms of two-component systems. Nat. Rev. Microbiol. *16*, 585–593. https://doi.org/10.1038/s41579-018-0055-7.

63. Croll, T.I. (2018). ISOLDE: a physically realistic environment for model building into low-resolution electron-density maps. Acta Crystallogr. D Struct. Biol. *74*, 519–530. https://doi.org/10.1107/S2059798318002425.

64. Mirdita, M., Schütze, K., Moriwaki, Y., Heo, L., Ovchinnikov, S., and Steinegger, M. (2022). ColabFold: making protein folding accessible to all. Nat. Methods *19*, 679–682. https://doi.org/10.1038/s41592-022-01488-1.

65. Wang, J., Wolf, R.M., Caldwell, J.W., Kollman, P.A., and Case, D.A. (2004). Development and testing of a general amber force field. J. Comput. Chem. *25*, 1157–1174. https://doi.org/10.1002/jcc.20035.

66. Jakalian, A., Jack, D.B., and Bayly, C.I. (2002). Fast, efficient generation of high-quality atomic charges. AM1-BCC model: II. Parameterization and validation. J. Comput. Chem. *23*, 1623–1641. https://doi.org/10.1002/jcc.10128.

67. Wang, J., Wang, W., Kollman, P.A., and Case, D.A. (2006). Automatic atom type and bond type perception in molecular mechanical calculations. J. Mol. Graph. Model. *25*, 247–260. https://doi.org/10.1016/j.jmgm.2005.12.005.

68. Altschul, S.F., Gish, W., Miller, W., Myers, E.W., and Lipman, D.J. (1990). Basic local alignment search tool. J. Mol. Biol. *215*, 403–410. https://doi.org/10.1016/S0022-2836(05)80360-2.

69. Henikoff, S., and Henikoff, J.G. (1992). Amino acid substitution matrices from protein blocks. Proc. Natl. Acad. Sci. USA *89*, 10915–10919. https://doi.org/10.1073/pnas.89.22.10915.

70. Madeira, F., Pearce, M., Tivey, A.R.N., Basutkar, P., Lee, J., Edbali, O., Madhusoodanan, N., Kolesnikov, A., and Lopez, R. (2022). Search and sequence analysis tools services from EMBL-EBI in 2022. Nucleic Acids Res. *50*, W276–W279. https://doi.org/10.1093/nar/gkac240.

71. Thompson, J.D., Higgins, D.G., and Gibson, T.J. (1994). CLUSTAL W: improving the sensitivity of progressive multiple sequence alignment through sequence weighting, position-specific gap penalties and weight matrix choice. Nucleic Acids Res. *22*, 4673–4680. https://doi.org/10.1093/nar/22.22.4673.

72. Capella-Gutiérrez, S., Silla-Martínez, J.M., and Gabaldón, T. (2009). trimAl: a tool for automated alignment trimming in large-scale phylogenetic analyses. Bioinformatics *25*, 1972–1973. https://doi.org/10.1093/bioinformatics/btp348.

Please cite this article in press as: Bódizs et al., Cryo-EM structures of a bathy phytochrome histidine kinase reveal a unique light-dependent activation mechanism, Structure (2024), https://doi.org/10.1016/j.str.2024.08.008

STAR★METHODS

KEY RESOURCES TABLE

REAGENT or RESOURCE	SOURCE	IDENTIFIER
Bacterial and virus strains		
Escherichia coli BL21 (DE3)	New England Biolabs	NCBI:txid469008
Chemicals, peptides, and recombinant proteins		
LB broth	VWR International AB	ICNA113002036
Critical commercial assays		
Zn^{2+}-Phos-tag® SDS-PAGE assay	Wako Chemicals	#AAL-107
Deposited data		
Raw images and curated particles	This paper	EMPIAR-12093
Pr density map (composite)	This paper	EMD-19981
Pr density map (consensus)	This paper	EMD-50007
Pr density map (PSM)	This paper	EMD-50008
Pr density map (OM)	This paper	EMD-50009
Pfr density map	This paper	EMD-19989
Pr model	This paper	9EUT
Pfr model	This paper	9EUY
Recombinant DNA		
pET28a(+) - *Pa*BphP	GenBank	AAG07504.1
Oligonucleotides		
*Pa*BphP forward cloning primer: ATCAATTC GGTCATATGATGACGAGCATCACCCCGG	This paper	N/A
*Pa*BphP reverse cloning primer: GAACAGCT GCCTCGAGTCAGGACGAGGAGCCGGT	This paper	N/A
Software and algorithms		
CryoSparc v4.2.1	Structura Biotechnology	cryosparc.com/
ISOLDE v1.5	Croll[63]	tristanic.github.io/isolde/
ChimeraX v1.5	UCSF	www.cgl.ucsf.edu/chimerax/
ColabFold v1.5.5	Mirdita et al.[64]	colab.research.google.com/github/sokrypton/ColabFold/blob/main/AlphaFold2.ipynb
BLAST	NCBI	blast.ncbi.nlm.nih.gov/Blast.cgi
Clustal Omega	EMBL-EBI	www.ebi.ac.uk/jdispatcher/msa/clustalo
Clustal W	EMBL-EBI	www.genome.jp/tools-bin/clustalw
trimAl	Capella-Gutiérrez et al.[72]	http://trimal.cgenomics.org/

RESOURCE AVAILABILITY

Lead contact

Further information and requests for resources and reagents should be directed to and will be fulfilled by the lead contact, Sebastian Westenhoff (sebastian.westenhoff@kemi.uu.se).

Materials availability

This study did not generate new unique reagents.

Data and code availability

- The data that support this study are available from the corresponding authors upon request. Raw microscopy images have been deposited in EMPIAR (EMPIAR-12093). EM density maps are available in EMDB: EMD-19989 (Pfr), EMD-19981 (Pr composite map), EMD-50007 (Pr consensus refinement), EMD-50008 (Pr photosensory module local refinement), EMD-50009 (Pr output module local refinement). PDB codes for the reconstructed models are 9EUY (Pfr) and 9EUT (Pr). They are publicly

Please cite this article in press as: Bódizs et al., Cryo-EM structures of a bathy phytochrome histidine kinase reveal a unique light-dependent activation mechanism, Structure (2024), https://doi.org/10.1016/j.str.2024.08.008

available as of the date of publication. Accession numbers corresponding to the reported structures are also listed in the key resources table.

- This paper does not report original code.

EXPERIMENTAL MODEL AND STUDY PARTICIPANT DETAILS

Source of the protein sample

The plasmid used for the recombinant expression of the full-length phytochrome from *P. aeruginosa* consists of the *Pa*BphP insert (GenBank: AAG07504.1) flanked by a C-terminal His6-tag, and the pET28a(+) plasmid backbone (Novagen). The heme oxygenase plasmid used to provide sufficient biliverdin incorporation during protein expression was kindly provided by Prof. Janne A. Ihalainen.

Growth conditions for the bacterial cultures

Double-transformed *Escherichia coli* strain BL21 (DE3) cells were cultured in LB media supplemented with 50 μg/mL kanamycin at 37°C until OD_{600} reached value 0.6. 1 mM IPTG and 5-aminolevulinic acid were added to induce expression of *Pa*BphP and heme oxygenase, and to aid biliverdin synthesis, respectively. Protein expression was done overnight at 18 °C.

METHOD DETAILS

Protein purification

Following cell lysis in lysis buffer (50 mM Tris, 150 mM NaCl, 10% glycerol, 10 U/mL of DNase 1 and one tablet of cOmplete EDTA-free protease inhibitor (Roche) at pH 8.0) using an EmulsiFlex C3 homogeniser (Avestin), the lysate was briefly incubated with a molar excess of biliverdin hydrochloride. The His6-tagged protein was then purified using Ni-NTA affinity chromatography (HisTrap HP 5 mL, Cytiva) by washing the bound sample with wash buffer (50 mM Tris and 1 M NaCl at pH 8.0) and eluting with elution buffer (50 mM Tris, 50 mM NaCl, 300 mM imidazole at pH 8.0); followed by size-exclusion chromatography (HiLoad 16/600 Superdex 200 pg, Cytiva) in SEC buffer (30 mM Tris at pH 8.0). The purified protein was collected at a concentration of 3 mg/mL and flash-frozen for storage.

Spectroscopy

The spectroscopic measurements (see Figure S1) were conducted using an AvaSpec-ULS2048CL-EVO (Avantes) spectrometer in combination with an Avalight-XE-HP (Avantes) light source, in a quartz cuvette with 10 mm light path. The protein sample was kept in complete darkness for 24 h for the dark state spectrum. For the far-red illuminated spectrum, the sample was illuminated with a 780-nm LED light source with a total energy of 1 mJ/mm^2. Dark reversion time was measured at room temperature, by recording spectra of the protein in dark at regular intervals immediately after far-red illumination. The degree of Pr content was determined by the absorption intensity at 700 nm.

Phos-tag assay

As the cognate RR of *Pa*BphP is not known, the Phos-tag assay was conducted with the RR from *D. radiodurans* (*Dr*RR). To generate phosphorylated *Dr*RR (p-*Dr*RR), *Dr*RR was pre-treated with 50 mM acetyl phosphate, as described previously.[30] Both kinase and phosphatase reactions were carried out in a buffer solution (25 mM Tris/HCl pH 7.8, 5 mM $MgCl_2$, 4 mM 2-mercaptoethanol, 5% ethylene glycol) with *Pa*BphP and *Dr*RR/p-*Dr*RR (2–4 μg each). The reactions were initiated by adding 1 mM ATP to the mixture and incubated at 25 °C, either in the dark or under saturating far-red (785 nm) light, for 20–30 min. The reactions were halted by adding 5*SDS-PAGE loading buffer. For the detection of p-*Dr*RR amount via mobility shift, we employed the Zn^{2+}-Phos-tag SDS-PAGE assay (Wako Chemicals) according to manufacturer's instructions. The samples were run with 40 mA in 9% SDS-PAGE gels containing 50 μM Phos-tag acrylamide at room temperature.

Sample preparation for cryo-electron microscopy

Prior to grid preparation, the protein buffer was exchanged to a solution containing 80 mM Tris, 10 mM $MgCl_2$ and 150 mM CH_3CO_2K with a pH of 7.8, and the protein concentration was set to 1.5 mg/mL. The protein was handled under dim 530-nm illumination during the preparation of dark Pfr state samples. For Pr state samples, an additional illumination step with a 780 nm light source (1 mJ/mm^2) was performed immediately before applying the solution on the grids (<10 s before freezing).

UltrAuFoil (Quantifoil) R 1.2/1.3 (300 mesh) grids were glow discharged for 60 s in an easiGlow (Pelco) glow discharge cleaning system before applying 3 μL protein solution and freezing in liquid ethane using a Vitrobot mark IV (Thermo Scientific), set to 100% humidity and 4°C.

Cryo-electron microscopy data collection

The prepared grids were loaded in a Titan Krios G2 (Thermo Scientific) transmission electron microscope equipped with a K3 (Gatan) detector and a 20 eV BioQuantum (Gatan) energy filter, operated at 300 keV. Data were collected with the following settings: 0.828 Å/pixel (105kx magnification), 50 e^-/Å^2 total electron dose, −0.8 to −2.0 μm defocus range. Automated collection was

performed using the EPU software (Thermo Scientific). A total of 30,336 movies were collected for the Pr state, and 15,496 movies for the Pfr state.

Cryo-electron microscopy data processing

The micrographs were processed using Cryosparc v4.2.1 (Structura Biotechnology). The movies were pre-processed by patch motion correction and patch CTF estimation, and low quality micrographs were discarded based on CTF fit, relative ice thickness and average intensity. Initial particle picking was done using blob picking for both datasets.

In the Pr dataset, different views of the closed conformation were used for template picking, and a Topaz model was trained on a clean particle set for the final round of picking. After *ab initio* reconstruction and heterogeneous refinement, a set of 889,461 particles was used for local refinement of the photosensory module. 3D variability analysis was used to uncover the structural heterogeneity. Further 3D classification of the particle set resulted in a subset of 179,058 particles, which were used to reconstruct the output module using non uniform refinement. An initial molecular model was aligned to the two structures, and the Phenix function 'Combine focused maps' was used to generate a composite map.

In the Pfr dataset, initial reconstructions were built for both the open and the closed conformations, and separate Topaz models were trained to pick particle sets for either conformation. The low number of total particles has prevented the reconstruction of a high resolution closed conformation structure. For the open state, *ab initio* reconstruction and heterogeneous refinement has resulted in a set of 1,103,315 particles. 3D variability analysis was used to uncover the structural heterogeneity. Further 3D classification has resulted in a subset of 239,820 particles, which were used for the final reconstruction using non-uniform refinement followed by local refinement.

Model building and refinement

Models for both the Pr and Pfr state were built using the ISOLDE (v1.5) extension of ChimeraX (v1.5).[63] An initial model was generated using ColabFold (v1.5.5), and the protomers were separately fitted into the density maps as rigid bodies.[64] To add biliverdin to the model, the GAFF force field in combination with the AM1-BCC charge model was used to generate the molecule LBV in antechamber.[65–67] The finished models were refined against the electron density maps using the Phenix (v1.20) function 'Real-space refinement'.

Multiple sequence analysis

BLAST was used on six different phytochrome sequences with the following Uniprot accession codes: *Dr*BphP (*D. radiodurans* - Q9RZA4), *Pa*BphP (*P. aeruginosa* - Q9HWR3), *Sa*BphP2 (*S. aurantiaca* - Q097N3), *Af*BphP (*A. fabrum* - Q7CY45), *En*FphA (*Emericella nidulans* - Q5K039) and Cph1 (*Syneochocystis* sp. PCC6803 - Q55168).[68] The E-Threshold was set to 0.1, the BLOSUM62 matrix was used and 250 hits per sequence with a minimum sequence identity of 30% were chosen.[69] Double hits were removed, which led to a total sequence number of 859 from 361 different families. The sequences were then aligned to the catalytic histidine in the output module.

MSA was performed using the Clustal Omega web server.[70] CLUSTAL W was used to generate the MSA.[71] Afterward, trimAl was used to cut the sequences at two reference positions, corresponding to residues L485 (within the PHY domain) and H513 (within the DHp domain) of *Pa*BphP.[72] The residues spanning the two reference positions were then counted and plotted as a histogram (Figure 6B), using an in-house python script.

QUANTIFICATION AND STATISTICAL ANALYSIS

Cryo-EM data collection and refinement statistics are summarized in Table S1.